Nonlinear Wavefield Characteristics of Seismic Translation and Rotation in Small-Strain Deformation: Insights from Moment Tensor Simulations

Wei Li [1,2], Yun Wang [1,2,*], Chang Chen[1,2], Lixia Sun[1,3]

[1] *"MWMC" group, School of Geophysics and Information Technology, China University of Geosciences, Beijing* 100083*, China*

[2] *State Key Laboratory of Geological Processes and Mineral Resources, China University of Geosciences, Beijing* 100083*, China*

[3] *Sinopec Research Institute of Petroleum Engineering Co., Ltd., Beijing* 102206*, China*

[*] Corresponding author: wangyun@mail.gyig.ac.cn.

Abstract Seismic rotational motions recorded in near-field and strong-magnitude observations exhibit discrepancies with theoretical predictions derived from linear elastodynamic principles. To explore potential nonlinear contributions to the phenomenon, this study incorporates nonlinear strain effects into wave propagation theory through Green-Lagrange strain tensor formulations. A staggered-grid finite-difference method simulates six-component wavefields (translational and rotational) generated by three fundamental seismic sources: isotropic (ISO), double-couple (DC), and compensated linear vector dipole (CLVD). Results demonstrate that nonlinear effects strongly depend on source characteristics and energy intensity. ISO sources exhibit uniform nonlinear anomalies from volumetric-shear coupling, CLVD sources amplify directional strain-axis effects, and DC sources amplify localized nonlinearity along faulting directions. Rotational components show higher sensitivity to nonlinearity than translational components, also contingent on source-receiver geometry. Simulations of two moderate-strong earthquakes highlight surface waves as preferential carriers of nonlinear signatures, though path effects and site amplification require systematic exploration. These results establish a framework for advancing nonlinearity study in ground motion analysis while emphasizing the need for instrumentally resolved rotational measurements and complex media modeling.

1 Introduction

Seismic rotational motions can be recorded in ground shaking, especially when caused by strong earthquakes (Graizer, 1991; 2010; Zhou et al., 2019). These rotational motions exhibit pronounced characteristics in shallow focal depths and near-field conditions (Kozak, 2009; Sun et al., 2017). Within the domain of structural engineering, the incorporation of rotational analysis has gained increasing recognition for its critical role in assessing ground motion stability and building design (Li, 1991; Li and Sun, 2001; Yan, 2017; Huras et al., 2021). Studies advancements suggest that incorporating seismic rotation data, which captures spatial gradients, can enhance the accuracy of earthquake source characterization and moment tensor inversion (Bernauer et al., 2014; Donner, 2016; Ichinose et al., 2021), as supported by simulations conducted by Hua and Zhang (2022).

The work of Lee (2007) comprehensively reviewed the applications of seismic rotation observations in seismic engineering, postulating that the measured rotation components in strong ground motion predominantly originate from the nonlinear elasticity and site effect. This conclusion is drawn from empirical evidence showing that actual rotational measurements exceed derived rotational components from translational data by 1-2 orders of magnitude. In addressing the complex geophysical phenomena stemming from Earth’s heterogeneities, progress has been made in developing analytical solutions for nonlinear wave equations through iterative techniques in Green’s function (McCall, 1994). Notable methodological developments include the flux-corrected transport method (Yang et al., 2002; Zheng et al., 2006) and perturbation approaches (Bataille and Contreras, 2009; Jia et al., 2020), which have been instrumental in investigating nonlinear effects on elastic wave propagation. However, current studies primarily focus on nonlinear constitutive relations between stress and strain under small strain and its linearization approximations (Renaud et al., 2012; 2013; TenCate et al., 2016; Feng et al., 2018), leaving a gap in understanding the strain nonlinearity. This aspect may hold the key to more accurate representations of rotational motions in strong earthquakes and near-field conditions.

In the seismically active region of Taiwan, broadband seismic observations and physical source studies have revealed significant rotational components in Taiwan's seismic events, demonstrating distinct strike-slip rotation characteristics between the southern and northern regions of the island (Yu et al., 1999; Wang and Lv, 2006). Oliveira and Bolt (1989) estimated rotational components of strong motions, confirming their non-negligible impact in near-field observations across Taiwan. Through analysis of six-component ground motion data from 52 earthquakes recorded at the HGSD station in eastern Taiwan during 2007-2008, Chen et al. (2014) identified substantial vertical rotational motions in proximal seismic locations and notable differences in energy and spectral characteristics between horizontal and vertical rotational motions. These studies show the importance of seismic rotation analysis in elucidating Taiwan's subsurface structures and geodynamic processes.

In this research, we develop a theoretical and numerical framework for analyzing nonlinear seismic wave propagation through Green strain tensor formulations. We derive velocity-stress equations incorporating nonlinear strain coupling terms, employ a staggered-grid finite-difference method to simulate six-component wavefields, and examine nonlinear six-component (C) wavefield characteristics through numerical simulations of three fundamental seismic moment tensor sources. Additionally, we conduct theoretical simulations of focal mechanisms of near-field and strong earthquakes along the Taiwan coast, analyzing source-dependent nonlinear responses to establish foundational insights for guiding future observational data studies.

2 Theory and method

2.1 Elastodynamic theory

Consider an elastic medium in three-dimensional space under orthogonal Cartesian coordinate (Fig. 1). Let particle A at position **x** within the medium, with an adjacent particle B at **x**+d**x**. The infinitesimal line element connecting these particles has an initial length ds. When subjected to external force, the material element AB undergoes displacement $\boldsymbol{u}(\boldsymbol{x}, t)$, transitioning to new positions A' and B' at **x**' and **x**'+d**x**', respectively, with a deformed length ds'. This deformation comprises both rigid-body displacement and strain-induced distortion. The work performed by the external force manifests as kinetic energy from particle motion and potential energy stored through elastic deformation. The strain energy density can be quantified by the differential quadratic form of the line element's length variation given in Eq. (1).

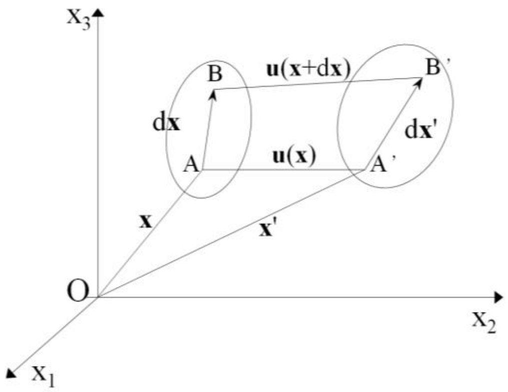

Figure 1. Schematic diagram of displacement and deformation of an elastic medium (Adapted from Aki and Richards (2002))

$$(ds')^2\text{-}(ds)^2 = 2E_{ij}dx_i dx_j,\ i, j \in \{1,2,3\} \tag{1}$$

where E_{ij} denotes the Green-Lagrange strain tensor components. All tensor equations adhere to the Einstein summation convention with dummy index notation. The displacement field u_i in Cartesian coordinate x_j defines the Green strain tensor (Eq. (2)), which provides an objective measure of deformation before and after external force application

$$E_{ij} = \frac{1}{2}(\frac{\partial u_j}{\partial x_i} + \frac{\partial u_i}{\partial x_j} + \frac{\partial u_k}{\partial x_i} \cdot \frac{\partial u_k}{\partial x_j}),\ i, j, k \in \{1,2,3\} \tag{2}$$

The displacement gradient tensor decomposes into symmetric strain (e_{ij}) and antisymmetric rotation (r_{ij}) components:

$$\frac{\partial u_j}{\partial x_i} = e_{ij} + r_{ij} \tag{3}$$

$$e_{ij} = \frac{1}{2}(\frac{\partial u_j}{\partial x_i} + \frac{\partial u_i}{\partial x_j}),\quad r_{ij} = \frac{1}{2}(\frac{\partial u_i}{\partial x_j} - \frac{\partial u_j}{\partial x_i}) \tag{4}$$

Conventional elastodynamic theory linearizes the Green strain tensor by neglecting second-order displacement gradient terms ($\partial u_k/x_i\, \partial u_k/x_j$), reducing it to the infinitesimal strain approximation:

$$E_{ij} \approx e_{ij} = \frac{1}{2}\left(\frac{\partial u_j}{\partial x_i} + \frac{\partial u_i}{\partial x_j}\right),\ i,\ j \in \{1,2,3\} \tag{5}$$

For isotropic elastic materials, the strain-stress relationship is given by:

$$\sigma_{ij} = \lambda\delta_{ij}e_{kk} + 2\mu e_{ij},\ i,j,k \in \{1,2,3\} \tag{6}$$

where λ and μ are Lamé coefficients, and δ_{ij} is the Kronecker delta. Incorporating nonlinearity through the complete Green strain tensor yields:

$$\begin{aligned}\sigma_{ij} &= \lambda\delta_{ij}E_{kk} + 2\mu E_{ij} \\ &= \lambda\delta_{ij}e_{kk} + 2\mu e_{ij} + \underbrace{\frac{1}{2}\lambda\delta_{ij}\left(\frac{\partial u_k}{\partial x_m}\cdot\frac{\partial u_k}{\partial x_m}\right) + \mu\frac{\partial u_k}{\partial x_i}\cdot\frac{\partial u_k}{\partial x_j}}_{\text{additional terms}},\ i,j,k,m \in \{1,2,3\}\end{aligned} \tag{7}$$

Substituting the nonlinear constitutive relation (Eq. (7)) into the momentum conservation law (Eq. (8)), where ρ is the material density.

$$\rho\frac{\partial^2 u_i}{\partial t^2} = \frac{\partial \sigma_{ij}}{\partial x_j},\ i,\ j \in \{1,2,3\} \tag{8}$$

Yields the nonlinear wave equation:

$$\begin{aligned}\rho\frac{\partial^2 u_i}{\partial t^2} &= \frac{\partial}{\partial x_j}\left(\lambda\delta_{ij}E_{kk} + 2\mu E_{ij}\right) \\ &= \underbrace{(\lambda+\mu)\frac{\partial^2 u_j}{\partial x_i \partial x_j} + \mu\frac{\partial^2 u_i}{\partial x_j \partial x_j}}_{\text{original terms}} + \underbrace{\lambda\frac{\partial u_k}{\partial x_i}\frac{\partial^2 u_k}{\partial x_j x_j} + \mu\left(\frac{\partial^2 u_k}{\partial x_i x_j}\frac{\partial u_k}{\partial x_j} + \frac{\partial^2 u_k}{\partial x_j x_j}\frac{\partial u_k}{\partial x_i}\right)}_{\text{additional terms}},\ i,j,k \in \{1,2,3\}\end{aligned} \tag{9}$$

In Eq. (9), the original terms correspond to the classical linear wave equation, while the additional terms arise from the nonlinear strain contributions. This reveals two fundamental nonlinear effects: (i) Volumetric nonlinearity (associated with λ): Coupling between shear deformation and volumetric strain. (ii) Shear nonlinearity (associated with μ): Interdependence of shear stress and principal strains. These additional third-order terms introduce complex interactions between deformation modes that are absent in linear theory. Their seismic manifestations depend critically on material properties and source characteristics, necessitating targeted numerical simulations to quantify nonlinear effects on wave propagation.

2.2 Staggered-grid finite-difference method

The staggered-grid finite-difference (SGFD) technique has proven effective for simulating seismic wave propagation. This method employs dual grid systems to discretize velocity-stress formulations, enabling stable computation of wavefield evolution in discrete spatial-temporal domains (Madariaga, 1976; Sun et al., 2018). As illustrated in Fig. 2, stress and velocity components are distributed across offset grid points to optimize numerical accuracy.

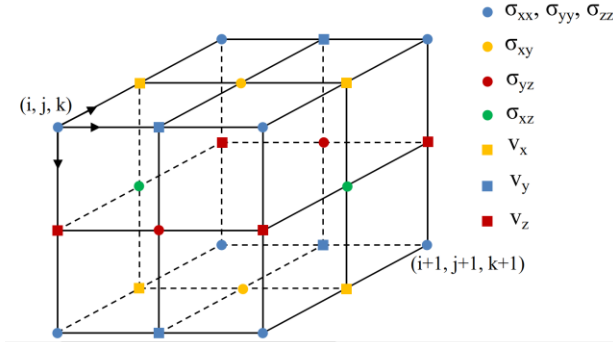

Figure 2. 3D staggered-grid configuration for velocity-stress formulations.

For 3D elastic isotropic media, we extend conventional linear strain formulations (Pei, 2005) by incorporating the nonlinear strain tensor E_{ij}. Temporal differentiation of the constitutive relation(Eq.(7)) yields velocity-stress relationships when combined with Eq. (8).

$$\begin{cases} \rho \dfrac{\partial v_i}{\partial t} = \dfrac{\partial \sigma_{ij}}{\partial x_j} \\ \dfrac{\partial \sigma_{ij}}{\partial t} = \lambda \delta_{ij} \dfrac{\partial E_{kk}}{\partial t} + 2\mu \dfrac{\partial E_{ij}}{\partial t} \\ \qquad = \lambda \delta_{ij} \dfrac{\partial v_k}{\partial x_k} + \mu \left(\dfrac{\partial v_i}{\partial x_j} + \dfrac{\partial v_j}{\partial x_i}\right) + \underbrace{\lambda \delta_{ij} \left(\dfrac{\partial v_k}{\partial x_m} \cdot \dfrac{\partial u_k}{\partial x_m}\right) + 2\mu \dfrac{\partial v_k}{\partial x_i} \cdot \dfrac{\partial u_k}{\partial x_j}}_{\text{additional terms}} \end{cases}, \quad i, j, k, m \in \{1, 2, 3\} \qquad (10)$$

where $v_i = \partial u_i / \partial t$(i ∈ {x, y, z}). Nonlinear contributions emerge through velocity-displacement coupling, whereupon take the displacement-preserving terms (u_i) as products of velocity components v_i and time dt (serve as time step in simulations) in the equations. In addition, rotation rates around Cartesian axes are derived from the antisymmetric rotation tensor (Eq. (4)).

Based on the equations, we implement these formulations through C/C++ code to numerically simulate seismic wave propagation. It contains perfectly matched layer (PML) boundaries to suppress boundary reflections (Dong and Ma, 2000) and acoustic boundary replacement (Eq. (13)) for free-surface implementation (Xu et al., 2007; Wang et al., 2012).

$$\begin{cases} \sigma^{0}{}_{zz} = 0 \\ \rho = 0.5\rho_0 \\ \lambda = 0 \\ \mu = \mu_0 \end{cases} \qquad (11)$$

where $\sigma^0{}_{zz}$, ρ, λ, and μ denote normal stress, medium density, and Lamé coefficients at and above the free surface, while ρ_0 and μ_0 represent density and Lamé coefficients below the free surface, respectively.

3 Simulations of basic seismic moment sources

3.1 Forward modelling parameters

Seismic moment tensors provide the most complete mathematical representation of point sources when the seismic wavelength exceeds the source dimension (Gilbert, 1970). As defined in Eq. (12), the symmetric second-order moment tensor **M** quantifies the equivalent force system acting at the hypocenter:

$$M_{ij} = \mu A(v_i n_j + v_j n_i),\ i, j \in \{1, 2, 3\} \tag{12}$$

Where μ is the shear modulus, A the fault area, v_i the slip vector, and n_j the fault normal vector. The tensor can be decomposed into three fundamental components: isotropy (ISO) component, double couple (DC) component, and compensated linear vector dipole (CLVD) component (Knopoff and Randall, 1970; Jost and Hermann, 1989). Specifically, the ISO component represents volumetric change with non-zero trace and uniform force along principal axes. The DC component signifies pure shear dislocation without volumetric change without volume variation. The CLVD component describes axial contraction/expansion with a dipole magnitude ratio 2:−1:−1. These moment tensor expressions can be written as shown below. These components govern distinct radiation patterns critical for understanding nonlinear seismic wave propagation effects.

$$\boldsymbol{M}^{ISO} = \begin{pmatrix} M_{11} & 0 & 0 \\ 0 & M_{22} & 0 \\ 0 & 0 & M_{33} \end{pmatrix}, \boldsymbol{M}^{DC} = \begin{pmatrix} 0 & M_{12} & 0 \\ M_{21} & 0 & 0 \\ 0 & 0 & 0 \end{pmatrix}, \boldsymbol{M}^{CLVD} = \begin{pmatrix} M_{11} & 0 & 0 \\ 0 & M_{22} & 0 \\ 0 & 0 & -2M_{33} \end{pmatrix} \tag{13}$$

Following Graves(1996), we implement moment tensor sources in the staggered-grid finite-difference scheme by converting body force to equivalent velocity sources. The loading equations for the three moment sources are shown in Eq. (14).

$$\boldsymbol{M}^{ISO}: \ \Delta v_i^n = \frac{M_{ij} \cdot dt \cdot f^n}{\rho V} \cdot \frac{\partial}{\partial x_j}$$
$$\boldsymbol{M}^{DC}: \ \Delta v_i^n = \frac{M_{jk} \cdot dt \cdot f^n}{\rho V} \cdot (\delta_{ij} \frac{\partial}{\partial x_k} + \delta_{ik} \frac{\partial}{\partial x_j}) \tag{14}$$
$$\boldsymbol{M}^{CLVD}: \ \Delta v_i^n = \frac{M_{kl} \cdot dt \cdot f^n}{\rho V} \cdot (\delta_{ik} \frac{\partial}{\partial x_l} + \delta_{il} \frac{\partial}{\partial x_k} - \frac{2}{3} \delta_{kl} \frac{\partial}{\partial x_i})$$

where i, j, k, $l \in \{1,2,3\}$. Δv denotes velocity increment, n the time step index, dt the time interval, ρ material density, and V grid cell volume. The source-time function f^n uses a Ricker wavelet with amplitude at $n \cdot dt$.

To exclude effects on nonlinear wave propagation from complex medium characteristics, we currently focus exclusively on simulations in a 3D homogeneous isotropic full-space model. The numerical implementation employs the Ricker wavelet with a 0.5 Hz dominant frequency. The model spans 80 km (x) × 80 km (y) × 80 km (z) with a uniform grid spacing of 500 meters in X, Y, and Z directions. Material properties are: P-wave velocity v_p=4400 m/s, S-wave velocity v_s=3000 m/s, and density ρ=2600 kg/m^3. The source resides at the model center (40 km, 40 km, 40 km). Temporal discretization uses Δt = 15 ms, with second-order differential accuracy in time and sixth-order in space.

For Numerical stability, based on the simulation parameters, the spatial discretization achieves 17.6 ($v_p/\Delta x \cdot f_{\mathrm{dominant}}$) points per wavelength for the dominant frequency, which exceeds the 8–10 PPW threshold for sixth-order schemes to suppress numerical dispersion artifacts (Virieux, 1986). Follows the temporal stability of 3D Courant-Friedrichs-Lewy (CFL) criterion ($\Delta t \cdot v_{\max} \cdot \mathrm{sqrt}(1/\Delta x^2+1/\Delta y^2+1/\Delta z^2)$), it reaches about 0.16. The resultant CFL number is a conservative value relative to the empirical 3D stability limit of 0.5 (Moczo et al., 2007), ensuring waveform fidelity while accommodating potential nonlinear term amplification.

3.2 Simulation results

3.2.1 ISO source

Fig. 3a displays 6C wavefield snapshots at 8 seconds for the ISO source under nonlinear deformation condition. Translational components exhibit uniform P-wave amplitudes, while rotational components show near absence of P-wave energy. The wavefield differences between linear and nonlinear simulations (Fig.3b) reveal emergent S-wave signatures, contrasting with classical elastodynamic theory where ISO sources exclusively generate P-waves in homogeneous isotropic media through pure compressional/expansional volume change. The anomalous P-S coupling phenomenon arises from nonlinear volumetric-shear strain interactions governed by the constitutive relationship (Eq. (7)), where the higher-order terms enable energy transfer between compressional and shear deformation modes.

Fig. 4 quantified the relative change between linear and nonlinear simulations at each grid cell volume. Where we applied a stability threshold to the relative change calculations to mitigate the influence of unrealistic wavefields ($value_{linear} \to 0$). It can be seen from Fig.4 that (i) the spatial distribution exhibits general symmetry and homogeneity with alternating positive/negative anomalies (Fig. 4a), where negative values (<0) indicate overestimation by linear theory and positive values (>0) suggest underestimation; (ii) rotational components have different and more complex azimuthal distribution and larger relative changes than translational components, also evidenced by probability density function (PDF) distributions in (Fig. 4b).

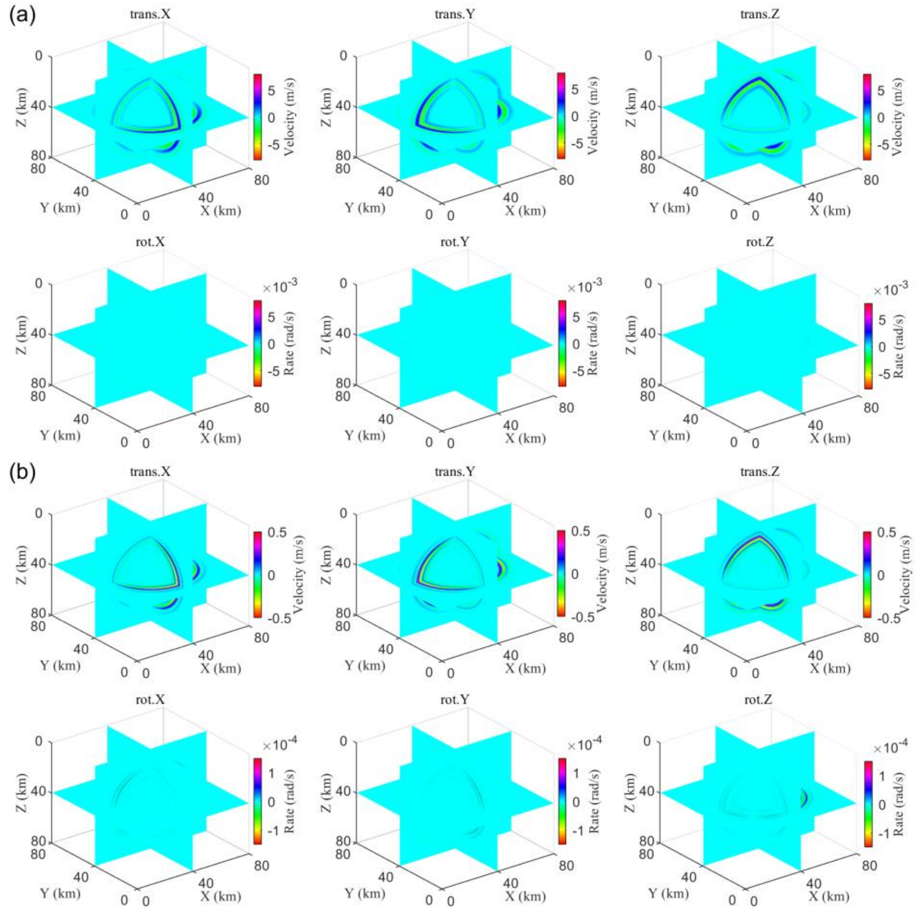

Figure 3. (a) Nonlinear 6C wavefield and (b) linear-nonlinear discrepancy for Mw7 ISO source at t=8s.

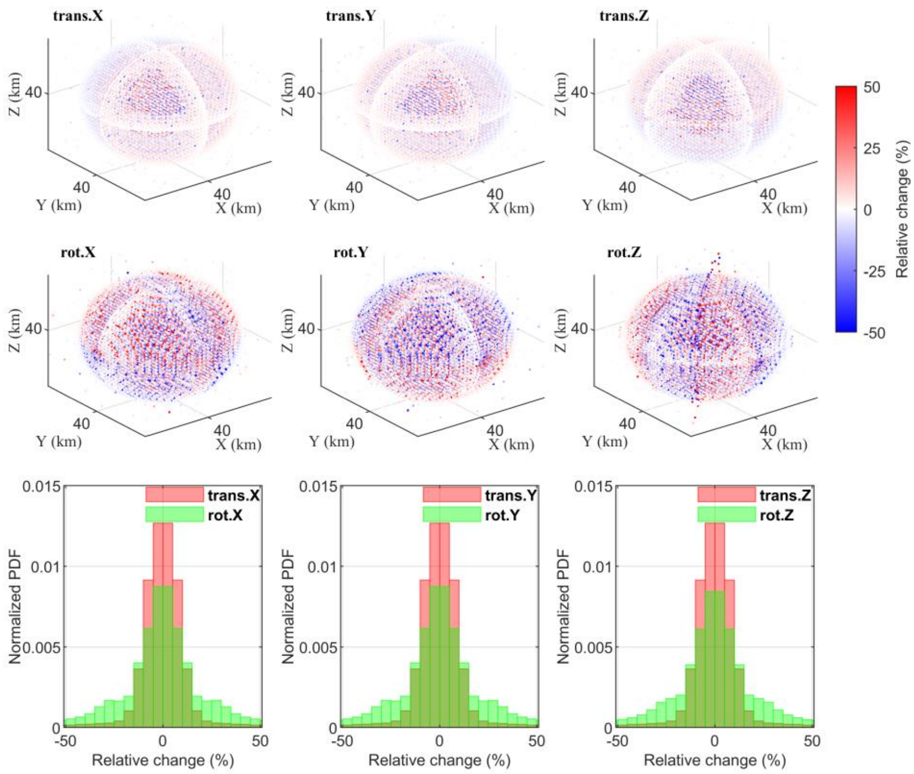

Figure 4. ISO source linear-nonlinear relative change: (a) 3D spatial distribution (b) Probability density function.

3.2.2 DC source

Fig. 5a presents 6C wavefield snapshots for the DC source under nonlinear conditions. The wavefield difference between nonlinear and linear wavefields in Fig. 5b demonstrates a different wavefront energy distribution from the original wavefront distribution in Fig. 5a. This energy redistribution caused by nonlinearity indicates that shear-dominated sources induce more complex nonlinear interactions.

The relative changes of nonlinear effects (Fig. 6) reveal not only zone variation but also localized strong nonlinearities at axial positions related to the distribution of the force couples tied to the DC source of fault displacement directions. At the same time, rotational components show a similar spatial distribution of underestimated and overestimated areas and localized strong nonlinearities, and rot.X and rot.Y components show larger change values, as seen from the PDF results.

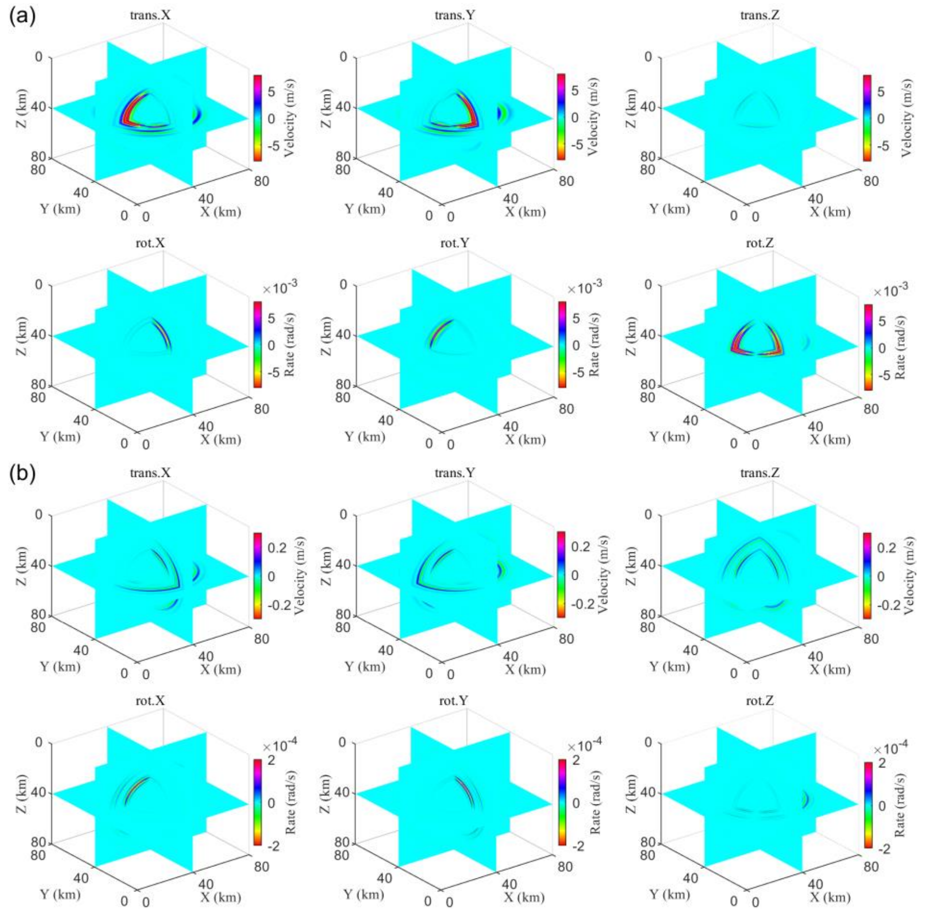

Figure 5. (a) Nonlinear 6C wavefield and (b) linear-nonlinear discrepancy for Mw7 DC source at t=8s.

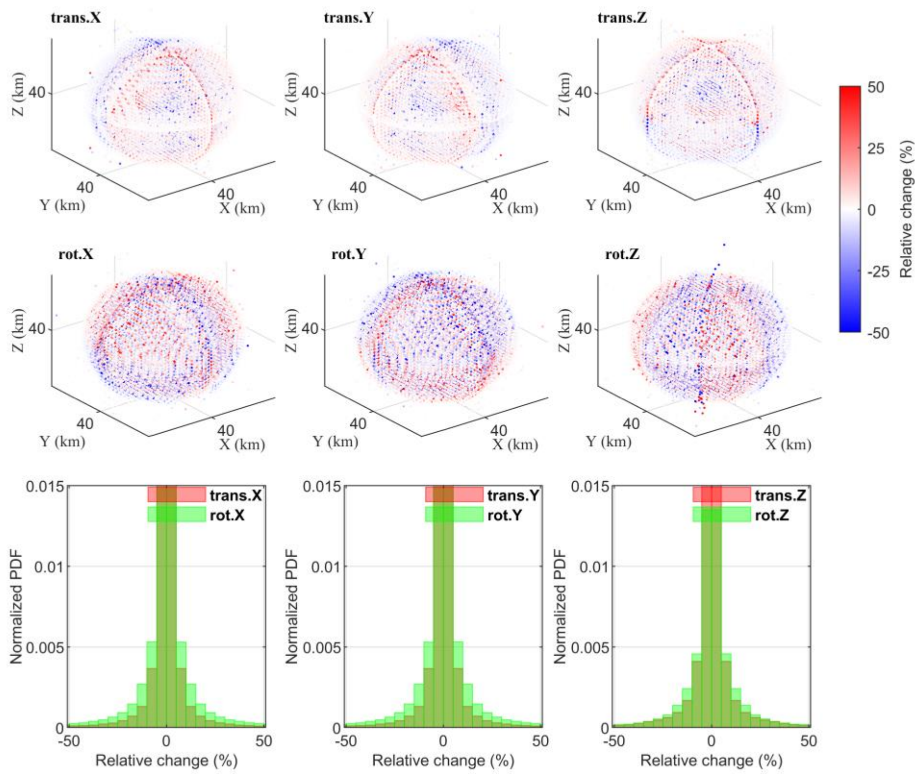

Figure 6. DC source linear-nonlinear relative change: (a) 3D spatial distribution (b) Probability density function.

3.2.3 CLVD source

Figs. 7 displays the results for the CLVD source simulation, demonstrating S-waves dominance in rotational components and its linear-nonlinear discrepancy in Fig. 7b highly resembles DC source results (Fig. 5b), reflecting their shared wavefield differences caused by nonlinearity for CLVD and DC source simulations may emerge from their fundamental kinematic similarity as non-volumetric source mechanisms.

Fig. 8 demonstrates Z-axis aligned anomalies corresponding to the CLVD compression axis for translational and rotational components, while the PDF distributions show overall enhanced nonlinear responses in rotational components.

The observed patterns correlate with the used CLVD source mechanism's kinematic characteristics — axial compression of twice the force along Z and extension in x/y directions — demonstrating how nonlinear effects inherit source radiation features while introducing directional dependence.

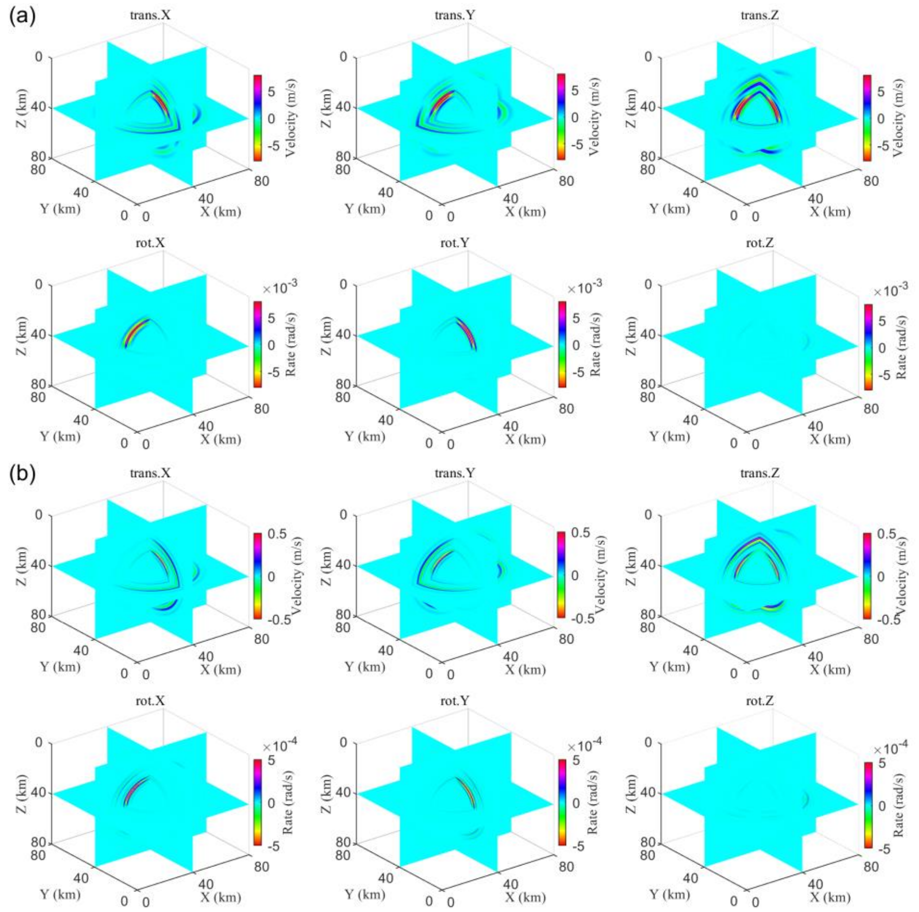

Figure 7. (a) Nonlinear 6C wavefield and (b) linear-nonlinear discrepancy for Mw7 CLVD source at t=8s.

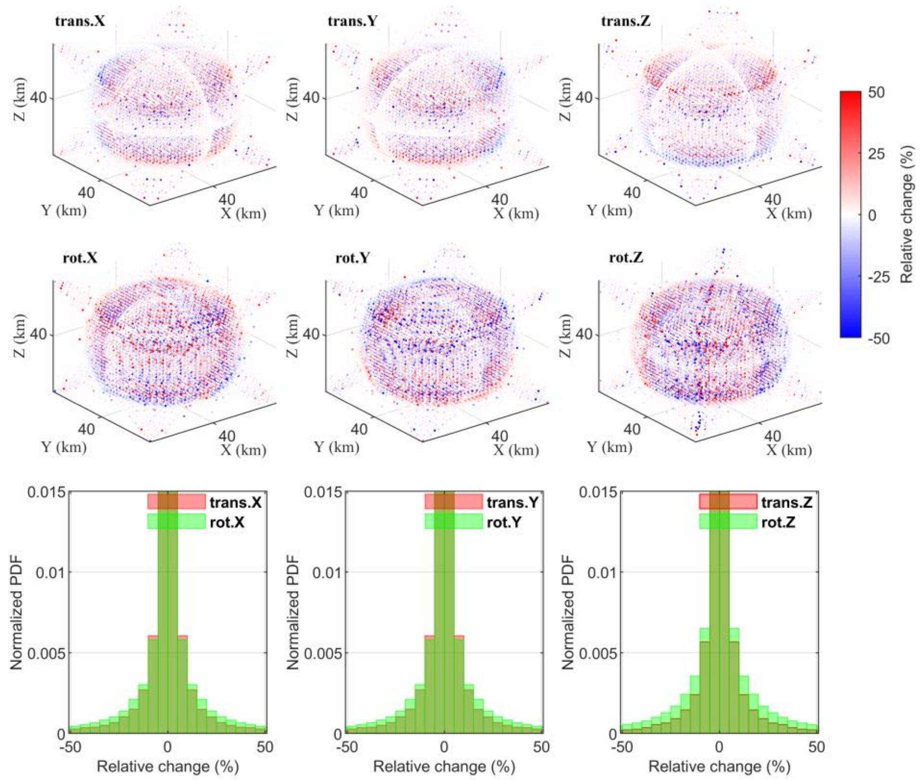

Figure 8. CLVD source linear-nonlinear relative change: (a) 3D spatial distribution (b) Probability density function.

The three force source types exhibit distinct nonlinear signatures governed by their fundamental characteristics. ISO sources generate more homogeneous spatial nonlinear effects. CLVD sources amplify directional nonlinear anomalies along principal strain axes. DC sources primarily restrict local stronger nonlinear effects to the force-couple axis. These differences emerge from how each source type interacts with the nonlinear strain tensor in Eq. (2). The cross-term $1/2\ \partial u_k/\partial u_i \cdot \partial u_k/\partial u_j$ enables energy transfer between deformation modes and violate the linear theory's strict P-S decoupling. Rotational components demonstrate particular sensitivity to these higher-order interactions, as evidenced by their broader PDF distributions across all source types. This source-dependent nonlinear behavior underscores the importance of considering rotational wavefield components and source kinematics when interpreting strong ground motions.

3.3 Wavefield comparisons

The nonlinear effects on seismic wavefields are qualified through relative energy change (ΔE) throughout the entire simulation domain using Eq. (15) and the sensitivity ratio of rotational to translational ($\Delta E_{rot}/\Delta E_{trans}$).

$$\Delta E = \frac{E_{nonlinear} - E_{linnear}}{E_{linnear}} \times 100\%, \ E = \sum_{i,j,k} v_{i,j,k}^2 \Delta V \qquad (15)$$

where $v_{i,j.k}$ is wavefield value at each grid point and ΔV is unit grid cell volume.

Fig. 9 illustrates the global energy variations between nonlinear and linear simulations at 6th seconds for ISO, CLVD, and DC sources. As the magnitude increases, the relative change of global wavefield energy shows an exponential increase, with sufficiently larger values of relative change when it reaches Mw 5. The ISO source exhibits the most pronounced nonlinear effects, with relative energy changes reaching 10.03% (translational) and 22.87% (rotational) at Mw7 (Fig. 9a, Table 1). This contrasts with CLVD and DC sources showing smaller changes (CLVD: 3.64% translational, 6.41% rotational; DC: <1% in all components).

The ISO source introduces uniform energy amplification in seismic components through nonlinear dilatational enhancing strain accumulation. The CLVD and DC sources redistribute localized energy, suppressing net energy changes, especially for the DC source.

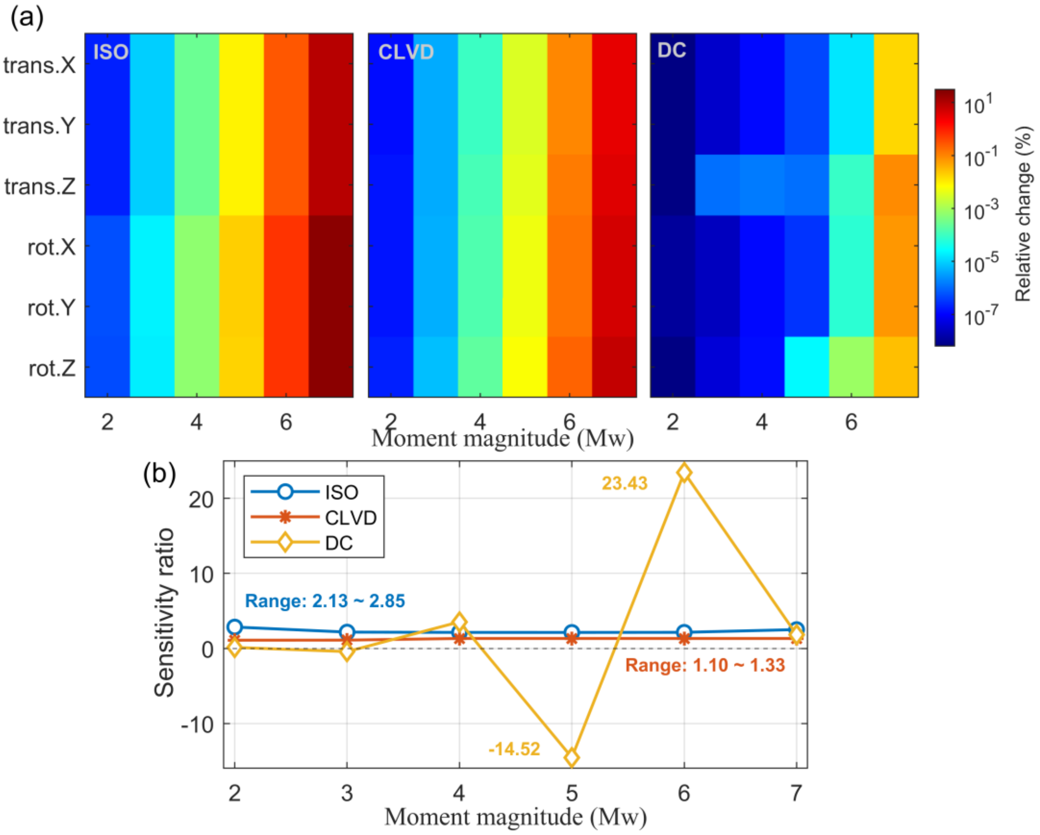

Figure 9. Relative energy changes induced by nonlinearity of (a) the three seismic sources at 6th second with increasing moment magnitude and sensitivity ratio of rotation vs. translation.

Table 1. Global wavefield energy change characteristics.

Source type	Max ΔE_{trans} (%, Mw7)	Max ΔE_{rot} (%, Mw7)	Sensitivity (rot./trans.)
ISO	10.03 (trans.)	22.87 (rot.)	2.13 ~ 2.85
CLVD	3.64 (trans.Z)	6.41 (rot.Z)	1.10 ~ 1.33
DC	0.03 (trans.Z)	0.09 (rot.Z)	extremes: -14.52, 23.43

The simulation results demonstrate that rotational measurements enhance nonlinear detection capability by 1-3× compared to traditional translational components. Current broadband seismometers possess sufficient resolution to detect these nonlinear wavefield anomalies. However, two critical constraints govern actual observational feasibility: magnitude-distance threshold and small/distant event challenges.

Pronounced nonlinear signatures manifest primarily in large-magnitude events (Mw $\geq$5) within near-field distances (simulated 30 km). This arises from strain amplitudes exceeding 10^{-4}—the empirical threshold for detectable nonlinear coupling (Guyer and Johnson, 1999), and limited geometric spreading and attenuation in proximal regions. For smaller magnitudes (Mw <5) or far-field observations, nonlinear strain amplitudes decay below, obscured by ambient noise floors, and path effects (scattering, attenuation) and source radiation patterns disperse nonlinear signatures. Given current instrumental limits (e.g., rotational sensor of a self-noise up to 2×10^{-8} $rad/s/\sqrt{Hz}$), targeted studies of near-field and moderate to strong earthquakes offer the most viable pathway to characterize nonlinear constitutive laws.

4 Earthquakes simulations

Building upon the theoretical framework for fundamental source types, we extend our simulations to more complex scenarios incorporating realistic source mechanisms and layered media. Analyzing two moderate-magnitude earthquakes (E1: Mw5.4 and E2: Mw6.1) along the Taiwan coast aims to validate theoretical predictions of nonlinear wave propagation and establish baseline understanding for future observational comparisons. The events were respectively recorded at stations NA01 (E1) and QS01 (E2) (Chen et al., 2023), as shown in Fig. 10 depicted by GMT (Wessel et al., 2019). Moment tensor solutions derived from the U.S. Geological Survey (USGS) are defined in Eq. (16), with synthetic 6C seismograms generated under both linear and nonlinear constitutive relations.

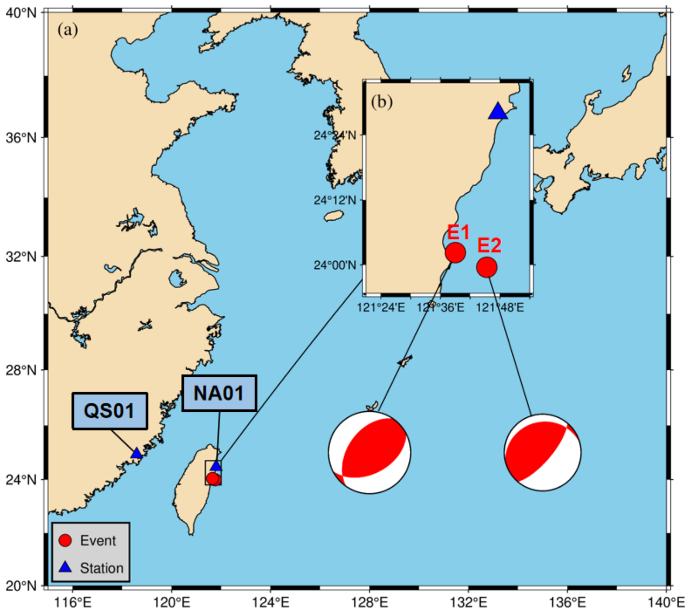

Figure 10. Epicenters and observation sites of E1 and E2

$$
\begin{aligned}
&E1:\begin{cases} M_{xx}=-7.569\times10^{16}, M_{yy}=-2.373\times10^{16}, M_{zz}=9.942\times10^{16} \\ M_{xz}=7.372\times10^{16}, M_{yz}=-1.0965\times10^{17}, M_{xy}=4.156\times10^{16} \end{cases} \\
&E2:\begin{cases} M_{xx}=-1.064\times10^{18}, M_{yy}=-7.607\times10^{17}, M_{zz}=1.8247\times10^{18} \\ M_{xz}=3.141\times10^{17}, M_{yz}=3.155\times10^{17}, M_{xy}=1.114\times10^{18} \end{cases}
\end{aligned} \tag{16}
$$

To isolate source-related nonlinearity, we simulate both earthquakes adopting the a simplified laterally homogeneous crustal model based on CRUST1.0 (Laske et al., 2013), with physical properties and simulation parameters listed in Tables 2 and 3. Free-surface condition is used at the top, and perfectly matched layer (PML) condition is used on other boundaries, with 10-order differential accuracy in space.

Table 2. Physical properties of layered media.

Layer	Thickness (km)	vp (km/s)	vs (km/s)	ρ (kg/m^3)
1	0.50	2.50	1.07	2.11
2	10.12	5.80	3.40	2.63
3	9.81	6.30	3.62	2.74
4	9.82	6.90	3.94	2.92
5	-	7.70	4.29	3.17

Table 3 Simulation parameters

Iterm	Paremeter (E1, E2)
Dominant frequency	1 Hz, 0.5 Hz
Moment magnitude	Mw5.4, Mw6.1
Depth	15 km, 30 km
Grid spacing	1 km, 2 km
Time step	5 ms, 2 ms
Source mechanisms	Eqs. (20), (21)
Spatial differential accuracy	10th order

Fig. 11a presents the simulated 6C seismic records for E1 in radial (R), transverse (T), and vertical (Z) coordinates, demonstrating prominent amplitude predominance in the trans.Z and rot.T components. Nonlinear effects manifest as subtle RMS amplitude changes (<1%), with rotational anomalies weaker than translational counterparts (Fig. 11b). Normalized time-frequency spectral differences further highlight distinct nonlinear patterns across components and wave phases: direct and reflected waves show larger RMS amplitude changes in trans.R and Z components, while surface waves in trans.T component display the strongest nonlinear sensitivity. S-waves in rot.R and T components and surface waves in rot.Z component show enhanced nonlinear effects, and Love-wave nonlinear perturbations in rot.Z component remain relatively weak.

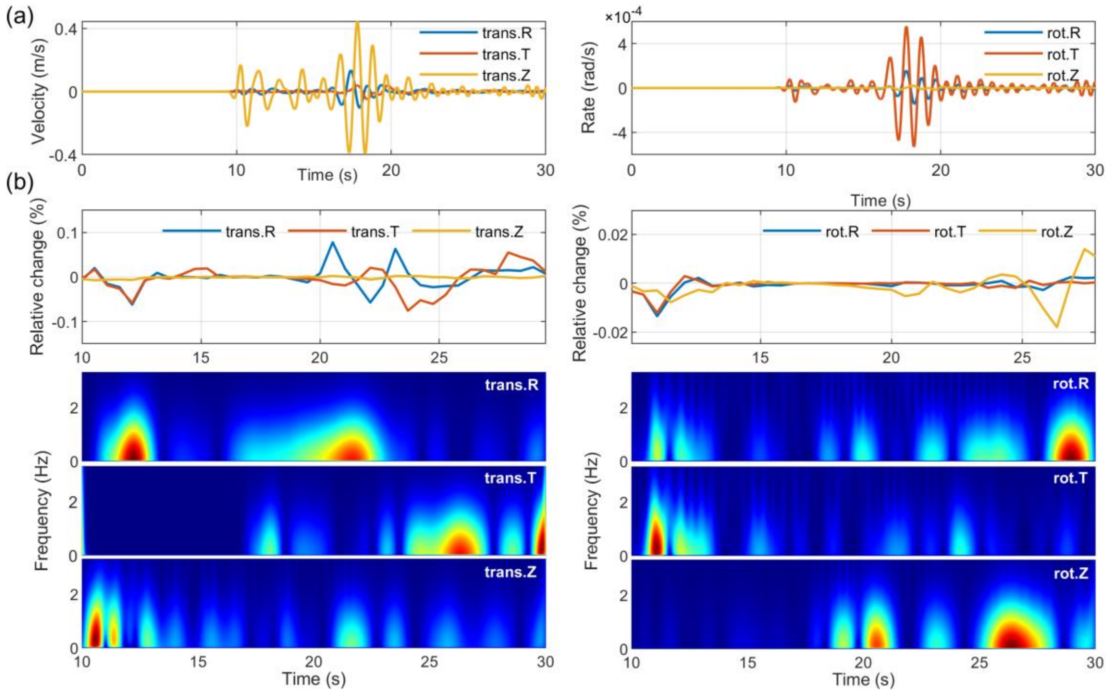

Figure 11. (a) Synthetic 6C seismic records under linear condition, and (b) Nonlinear-induced time-frequency spectral difference for E1.

The larger-magnitude E2 simulation demonstrates stronger nonlinear effects, particularly in trans.Z and rot.T components (Fig. 12). Rayleigh waves show pronounced nonlinear distortions, while P-waves in trans.Z and surface waves in trans.R and T components exhibit moderate changes. S-waves and surface waves in the rot.R component are also affected, though rot.Z waveforms display minimal nonlinear alterations.

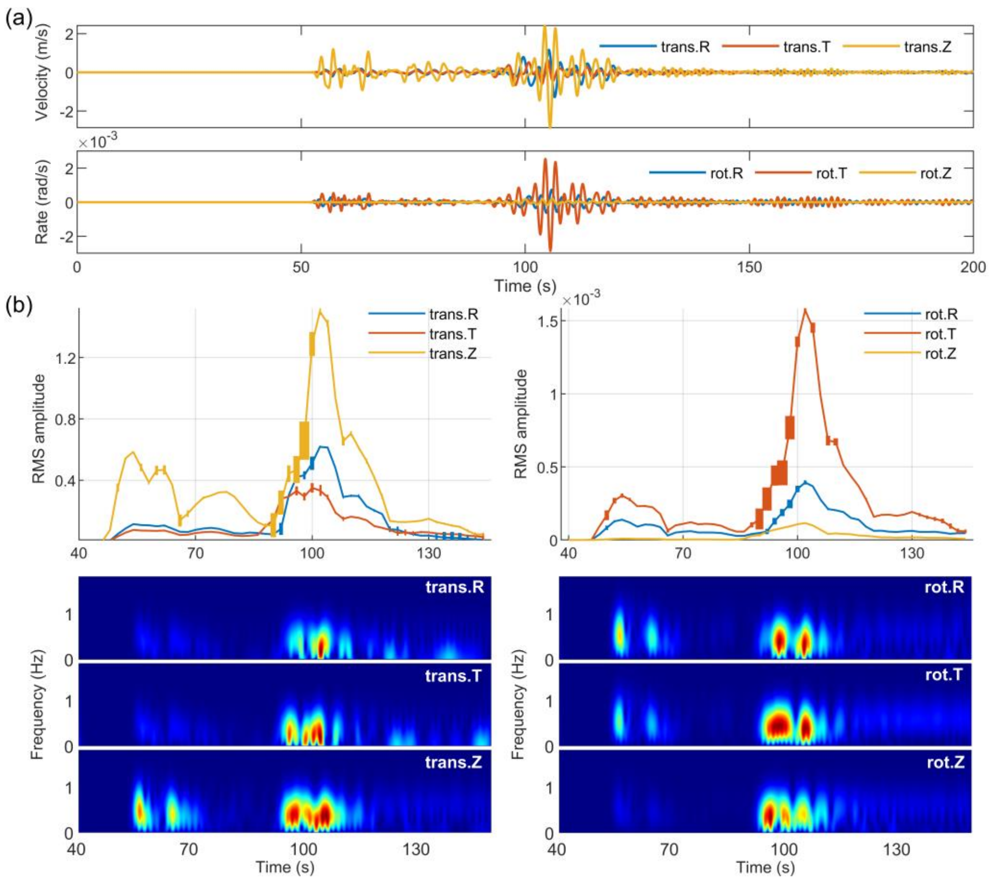

Figure 12. (a) Synthetic 6C seismic records under linear condition, and (b) Nonlinear-induced time-frequency spectral difference for E2.

The simulations of E1 and E2 reveal some observational implications. For E1, the weak nonlinear effects (<1% amplitude changes) suggest that its receiver location may lie in a region of suppressed nonlinear coupling, likely due to unfavorable source-receiver geometry. In contrast, E2 exhibits stronger nonlinear signatures, particularly in surface waves. This enhanced nonlinear sensitivity in surface waves arises from their inherent P-S interference characteristics, making it a more viable candidate for studying nonlinear effects.

While rotational Z-component Love waves show minor nonlinear alterations, the translational R/T components and rotational R/T components demonstrate more significant changes, particularly in Rayleigh waves. These findings emphasize the need to prioritize specific wave phases and components in future observational data studies. For practical applications, wavefield separation techniques may be necessary to isolate S-waves and surface waves in translational and rotational components, where nonlinear effects are most pronounced.

5 Discussion

The incorporation of Green strain tensor-based nonlinearity into classical elastodynamic theory introduces higher-order displacement gradient terms (Eqs. (7) and (9)), fundamentally altering seismic wave dynamics by coupling volumetric and shear deformation modes. In linear elasticity theory, volumetric (principal) and shear strains are completely decoupled, and P-wave and S-wave are driven by normal stresses and shear stresses, respectively. While ISO source simulation reveals P-S wave conversion through nonlinear dilatational-shear interactions, the real-world manifestation of such phenomena is constrained by multi-factor geological complexities absent in our idealized models. Future work should prioritize simulations incorporating velocity gradients and attenuation profiles to quantify how propagation paths modulate nonlinear effects, particularly for surface waves where site amplification may enhance nonlinear coupling.

The differences between E1 and E2 simulations further highlight the need to explore complex source characteristics. While E2's larger magnitude produced clearer nonlinear signatures, most natural earthquakes involve composite rupture dynamics and asymmetric moment tensors. Expanding simulations to include finite-fault sources and spatially varying rupture kinematics could reveal how source complexity interacts with nonlinear strain accumulation.

Finally, while rotational components show theoretical sensitivity to nonlinear effects, their practical utility remains constrained by observational challenges. Field rotational motions are inherently weaker than translations, and current instruments struggle to resolve most nonlinear changes. Addressing these limitations will require coordinated advances in sensor technology, wavefield separation methods, and targeted field observations focusing on moderate-strong earthquakes where nonlinear effects may cross detection thresholds.

6 Conclusions

This work establishes a theoretical and numerical framework for analyzing nonlinear seismic wave propagation through Green strain tensor strain tensor formulations. Numerical simulations of three fundamental seismic moment tensor sources (ISO, CLVD, DC) and two moderate-to-strong magnitude earthquakes yield the following key conclusions.

(i) Force-source-type dependency: The spatial distribution is intrinsically tied to source kinematics. ISO sources generate overall uniform nonlinear anomalies through volumetric-shear coupling, CLVD sources amplify directional anomalies along principal strain axes of compression/expansion, and DC sources restrict localized nonlinearity to fault-aligned force couple orientations. These patterns arise from how each force source geometry interacts with the nonlinear strain tensor.

(ii) Magnitude-energy relationship: Nonlinear effects scale exponentially with seismic moment, becoming observationally significant for magnitudes above Mw5. At Mw7, rotational components exhibit over 20% relative changes compared to linear predictions, whereas changes remain negligible for Mw <4 events. This underscores the importance of strain amplitude in triggering detectable nonlinear coupling.

(iii) Rotational motion sensitivity: Rotational components generally demonstrate higher nonlinear sensitivity than translational components. Their practical detectability depends on source-receiver azimuth.

(iiii) Wave-type specificity: Surface waves exhibit stronger nonlinear signatures than body waves in both earthquake simulations, likely due to their inherent P-S interference during propagation. However, current models inadequately address surface wave nonlinearity, suggesting unresolved interactions between nonlinear effects and site amplification.

Author contributions. WL: conceptualization, methodology, investigation, formal analysis, writing - original draft. YW: conceptualization, writing - original draft and revised draft. CC: investigation, formal analysis. LS: methodology.

Data and resources. The seismic records of **E**1 are provided by the Institute of Earth Sciences, Academia Sinica, Taiwan, China. The translational records of **E**2 are acquired from the Fujian Earthquake Agency.

Competing interests. The contact author has declared that neither of the authors has any competing interests.

Disclaimer. Publisher's note: Copernicus Publications remains neutral with regard to jurisdictional claims made in the text, published maps, institutional affiliations, or any other geographical representation in this paper.

Financial support. This research is financially supported by the National Natural Science Foundation of China (No. 42150201、No. 62127815、No. U1839208).

References

Aki, K., and P. G. Richards. Quantitative seismology, 2nd ed, California: University Science Books, https://doi.org/10.1029/2003EO210008, 2002.

Bataille, K., Contreras, M.: Nonlinear elastic effects on permanent deformation due to large earthquakes, Phys. Earth Planet. Inter., 175(1), 47-52, https://doi.org/10.1016/j.pepi.2008.02.016, 2009.

Bernauer, M., Fichtner, A., and Igel, H.: Reducing nonuniqueness in finite source inversion using rotational ground motions, J. Geophys. Res.-Solid Earth, 119(6), 4860-4875, https://doi.org/10.1002/2014JB011042, 2014.

Chen, C., Wang, Y., Sun, L. X., Lin, C. J., Wei, Y. x., Liao, C. Q., Lin, B. H.,and Qin, L. P.: Six-component earthquake synchronous observations across Taiwan Strait: Phase velocity and source location, Earth and Space Science, 10, e2023EA003040, https://doi.org/10.1029/2023EA003040, 2023.

Chen, Q. J., Yin, J. E., and Yang, Y. S.: Time-frequency characteristic analysis of six-degree-freedom ground motion records, Chinese Quarterly of Mechanics, 35, (3), 499-506, https://link.oversea.cnki.net/doi/10.15959/j.cnki.0254-0053.2014.03.033, 2014 (in Chinese).

Dong, L. G., and Ma, Z. T.: A staggered-grid high-order difference method of one-order elastic wave equation, Chinese J. Geophys., 43(3), 411-419, 2000 (in Chinese).

Donner, S., Bernauer, M., and Igel, H.: Inversion for seismic moment tensors combining translational and rotational ground motions, Geophys. J. Int., 207(1), 562-570, https://doi.org/10.1093/gji/ggw298, 2016.

Feng, X., Fehler, M., Brown, S., Szabo, T. L., and Burns, D.: Short-period nonlinear viscoelastic memory of rocks revealed by copropagating longitudinal acoustic waves, J. Geophys. Res.-Solid Earth, 123(5), 3993–4006, https://doi.org/10.1029/2017JB015012, 2018.

Graizer, V. M.: Strong motion recordings and residual displacements: what are we actually recording in strong motion seismology? Seismol. Res. Lett., 8(4), 635-639, https://doi.org/10.1785/gssrl.81.4.635, 2010.

Graizer, V. M.: Inertial seismometry methods, Earth Physics, 27(1), 51-61, 1991.

Graves, R. W.: Simulating seismic wave propagation in 3D elastic media using staggered-frid finite differences, Bull. Seismol. Soc. Am., 86(4), 1091-1106, 1996.

Gilbert, F.: Excitation of the normal modes of the Earth by earthquake sources, Geophys. J. R. astr. Soc, 22(2), 223-226, https://doi.org/10.1111/j.1365-246X.1971.tb03593.x, 1970.

Guyer, R. A., and Johnson, P. A.: Nonlinear mesoscopic elasticity: evidence for a new class of materials, Physics Today, 52(4), 30-36, https://doi.org/10.1063/1.882648, 1999.

Hua, S. B., and Zhang, Y.: Numerical experiments of moment tensor inversion with rotational ground motions, Chinese J. Geophys., 65(1), 197-213, https://doi.org/10.6038/cjg2022P0668, 2022 (in Chinese).

Huras, L., Zembaty, Z., Bonkowski, P. A., and Bobraet, P.: Quantifying local stiffness loss in beams using rotation rate sensors, Mech. Syst. Signal Proc., 151, 107396, https://doi.org/10.1016/j.ymssp.2020.107396, 2021.

Ichinose, G. A., Ford, S. R., and Mellors, R. J.: Regional moment tensor inversion using rotational observations, J. Geophys. Res.-Solid Earth, 126(2), e2020JB020827, https://doi.org/10.1029/2020JB020827, 2021.

Jia, L., Yan, S. G., Zhang, B. X., and Huang, J.: Research on perturbation method for nonlinear elastic waves, J. Acoust. Soc. Am., 148, EL289–EL294, https://doi.org/10.1121/10.0001980, 2020.

Jost, M. L., and Hermann, R. B.: A students guide to and review of moment tensors, Seism. Res. Lett., 60, 37-57, https://doi.org/10.1785/gssrl.60.2.37, 1989.

Knopoff, L., and Randall M. J.: The compensated linear-vector dipole: A possible mechanism for deep earthquakes, J. Geophy. Res., 75(26), 4957–4963, https://doi.org/10.1029/JB075i026p04957, 1970.

Kozak, J. T.: Tutorial on earthquake rotational effects: historical examples, Bull. Seismol. Soc. Am., 99(2B), 998-1010, https://doi.org/10.1785/0120080308, 2009.

Laske, G., Masters, G., Ma, Z. T., and Pasyanos, M.: Update on CRUST1. 0-A 1-degree global model of Earth's crust, EGU General Assembly 2013, 15, EGU2013-2658, 2013.

Lee, C. E. B., Celebi, M., Todorovska, M. I., and Diggles, M. F.: Rotational seismology and engineering applications — Proceedings for the First International Workshop, Menlo Park, California, U.S.A.—September 18 to 19, 2007: U.S. Geological Survey Open-File Report 2007-1144, 46 p. http://pubs.usgs.gov/of/2007/1144/, 2007.

Li, H. N.: Study on rotational components of ground motion, Journal of Shenyang Architectural and Civil Engineering Institute, 7(1), 88-93, 1991 (in Chinese).

Li, H. N., and Sun, L. Y.: Rotational components of earthquake ground motions derived from surface waves, Earthq. Eng. Eng. Vib., 21(1), 15-23, https://link.oversea.cnki.net/doi/10.13197/j.eeev.2001.01.003, 2001 (in Chinese).

Madariaga, R.: Dynamics of an expanding circular fault, Bull. Seismol. Soc. Am., 66(3), 639-666, https://doi.org/10.1007/BF02246368, 1976.

McCall, K. R.: Theoretical study of nonlinear elastic wave propagation, J. Geophys. Res., 99(B2), 2591-2600, https://doi.org/10.1029/93JB02974, 1994.

Moczo, P., Robertsson, O. J., and Eisner, L.:The finite-difference time-domain method for modeling of seismic wave propagation, Advances in Geophysics, 48, 421-516. https://doi.org/10.1016/S0065-2687(06)48008-0, 2007.

Oliveira, C. S., and Bolt, B. A.: Rotational components of surface strong ground motion, Earthq. Eng. Struct. D. 18(4), 517–526, https://doi.org/10.1002/eqe.4290180406, 1989.

Pei, Z. L.: Numerical simulation of elastic wave equation in 3-D anisotropic media with staggered-grid high-order difference method, Geophysical Prospecting for Petroleum, 44(4), 308-315, https://doi.org/10.3969/j.issn.1000-1441.2005.04.002, 2005 (in Chinese).

Renaud, G., Le Bas, P. Y., and Johnson, P. A.: Revealing highly complex elastic nonlinear (anelastic) behavior of Earth materials applying a new probe: Dynamic acoustoelastic testing, J, Geophys. Res.-Solid Earth, 117, B06202, , https://doi.org/10.1029/2011JB009127, 2012.

Renaud, G., Rivière, J., Le Bas, P. Y., and Johnson, P. A.: Hysteretic nonlinear elasticity of Berea sandstone at low-vibrational strain revealed by dynamic acoustoelastic testing, Geophys. Res. Lett., 40(4), 715-719, https://doi.org/10.1002/grl.50150, 2013.

Sun, L., Yu, Y., Lin, J. Q., and Liu, J. L.: Study on seismic rotation effect of simply supported skew girder bridge, Earthquake Engineering and Engineering Dynamics, 37(4), 121-128, https://doi.org/10.13197/j.eeev.2017.04.121.sunl.014, 2017 (in Chinese).

Sun, L. X., Zhang, Z., and Wang, Y.: Six-component elastic-wave simulation and analysis, EGU General Assembly 2018, Geophysical Research Abstracts, 20, EGU2018-14930-1, 2018.

TenCate, J. A., Malcolm, A. E., Feng, X., and Fehler, M. C.: The effect of crack orientation on the nonlinear interaction of a P wave with an S wave, Geophys. Res. Lett., 43(12), 6146-6152, https://doi.org/10.1002/2016GL069219, 2016.

Virieux, J.: P-SV wave propagation in heterogeneous media; velocity-stress finite-difference method, Geophysics, 51(4), 889-901, https://doi.org/10.1190/1.1442147, 1986.

Wang, L., Luo, Y. H., and Xu, Y. H.: Numerical investigation of Rayleigh-wave propagation on topography surface, J. Appl. Geophys., 86, 88–97, https://doi.org/10.1016/j.jappgeo.2012.08.001, 2012.

Wessel, P., Luis, J. F., Uieda, L., Scharroo, R., Wobbe, F., Smith, W. H. F., and Tian, D.: The generic mapping tools version 6, Geochemistry, Geophysics, Geosystems, 20, 5556–5564, https://doi.org/10.1029/2019GC008515, 2019.

Xu, Y. X., Xia, J. H., and Miller, R. D.: Numerical investigation of implementation of airearth boundary by acoustic-elastic boundary approach, Geophysics, 72 (5), SM147–SM153, https://doi.org/10.1190/1.2753831, 2007.

Yan, Y. Y.: Seismic response analysis of high-rise building under different types of multi-dimensional earthquake ground motions (Ph.D. dissertation), Jiangsu University, 2017(in Chinese).

Yu, S. B., Kuo, L. C., and Punongbayan, R. S., Emmanuel, G.R.: GPS observation of crustal deformation in Taiwan-Luzon region, Geophys. Res. Lett., 26(7), 923-926, https://doi.org/10.1029/1999GL900148, 1999.

Yang, D. H., Liu, E., Zhang, Z.J., and Teng, J.: Finite-difference modelling in two-dimensional anisotropic media using a flux-corrected transport technique, Geophys. J. Int., 148(2), 320–328, https://doi.org/10.1046/j.0956-540x.2001.01575.x, 2002.

Zheng, H. S., Z. J. Zhang, and Liu, E. R.: Nonlinear seismic wave propagation in anisotropic media using the flux-corrected transport technique, Geophys. J. Int., 165(3), 943-956, https://doi.org/10.1111/j.1365-246X.2006.02966.x, 2006.

Zhou, C., Zeng, X. Z., Wang, Q. L., and Liu, W. Y., and Wang, C. Z.: Rotational motions of the Ms7.0 Jiuzhaigou earthquake with ground tilt data, Science China Earth Science, 62(5), 832-842, https://doi.org/10.1007/s11430-018-9320-3, 2019.